

# Data-oriented strategy and $V_p/V_s$ model-constraint for simultaneous $V_p$ and $V_s$ reconstruction in 3D visco-elastic FWI: Application to the SEAM II Foothill dataset.

P.T. Trinh<sup>1,2</sup>, R. Brossier<sup>2</sup>, L. Métivier<sup>2,3</sup>, J. Virieux<sup>2</sup>

<sup>1</sup> Total E&P, <sup>2</sup> Univ. Grenoble Alpes, ISTERre, <sup>3</sup> Univ. Grenoble Alpes, CNRS, LJK

## SUMMARY

Full waveform inversion (FWI) of onshore targets is very challenging due to the complex free-surface-related effects and 3D geometry representation. In such areas, the seismic wavefield is dominated by highly energetic and dispersive surface waves, converted waves and back-scattering energy. We use a time-domain spectral-element-based approach for elastic wavefield simulation in foothill areas. The challenges of the elastic multi-parameter FWI in complex land areas are highlighted through the inversion of the pseudo-2D dip-line survey of the SEAM Phase II Foothill dataset. As the data is dominated by surface waves, it is mainly sensitive to the S-wave velocity. We then propose a two-steps data-windowing hierarchy to simultaneously invert for P- and S-wave speeds, focusing on early body waves before considering the whole data. By doing so, we aim at exploiting the maximum amount of information in the observed data and getting a reliable model parameters estimation, both in the near-surface and in deeper part. The model constraint that we introduce on the ratio of compressional and shear velocities also plays an important role to mitigate the ill-posedness of the inversion process.

## INTRODUCTION

Full waveform inversion (FWI) for onshore targets is very challenging due to complex free-surface-related effects and 3D geometry representation. In such areas, the seismic wavefield is dominated by highly energetic and dispersive surface waves, converted waves and back-scattering energy when the waves hit the steep slopes at the surface, or strong velocity contrasts. These complex effects cannot be fully removed or compensated by data pre-processing, implying that a correct description of the physics is strongly advisable for accurate model parameters estimation. Moreover, considering the complete physical phenomena of the wave propagation would make possible to take benefit of each piece of recorded data, for expected more accurate results and higher resolution. Adequate geometry representation is also required to honor the interaction between elastic waves and geological structures such as rapid topography variation and erosions. When considering complex structures or geological heterogeneities, regularization and preconditioning strategies also play an important role to mitigate the ill-posedness of the inversion problem (Guitton et al., 2012).

The SEAM Phase II Foothill model and dataset are created by the SEAM consortium to reproduce the imaging challenges in mountain regions (Regone et al., 2017). Starting from relatively crude initial models, we focus on the simultaneous reconstruction of compressional and shear waves velocities from the pseudo-2D dip-line visco-elastic survey. Beside the poor illumination of the pseudo-2D acquisition, the task is particu-

larly difficult due to the strong near-surface heterogeneities and complex geometries.

In our study, the 3D elastic and viscoelastic FWI is performed using our code SEM46 (Spectral Element Method for Seismic Imaging in eXploration), which is based on a time-domain spectral element method (SEM). We highlight the importance of data-windowing hierarchy and model constraint for simultaneous reconstruction of  $V_p$  and  $V_s$ . We show that it is possible to reconstruct the shallow part form early-body waves before integrating surface waves for better constraining the construction at depth.

## WAVE PROPAGATION AND FWI IN SEM46

SEM46 uses a classical hexahedra-based SEM frame for elastic and viscoelastic modeling (Komatitsch and Tromp, 1999). The physical domain is represented by a flexible Cartesian-based deformed mesh with high-order geometry representation to capture complex topographies and variable element-size to reduce the numerical cost. The viscoelastic wave propagation is performed under the approximation of constant quality factors  $Q_p$  and  $Q_s$ , which are represented by a set of standard-linear-solid mechanisms over the seismic frequency band (Yang et al., 2016; Trinh et al., 2018). The wavefield at the boundary is absorbed by a combination of sponge layers (Cerjan et al., 1985) and radiative boundary condition (Stacey, 1988). The inversion is based on the minimization of the least-squares norm between the observed and the calculated data. Various non-linear optimization methods, coupled with the same line-search algorithm, are embedded through the SEISCOPE optimization toolbox (Métivier and Brossier, 2016). The FWI gradient, required as the input of the optimization process, is computed following the adjoint approach. The gradient preconditioning is directly performed on the SEM mesh, by using the structurally-based nonstationary and anisotropic Bessel smoothing filter (Trinh et al., 2017). The filter shape is defined by variable coherent lengths:  $L_v(\mathbf{x})$  is associated with the direction perpendicular to the local bedding plan,  $L_u(\mathbf{x})$  and  $L_w(\mathbf{x})$  are related to the planar structure of potential geological features. The 3D orientation is controlled by azimuth and dip angles.

### Model constraint on the ratio $V_p/V_s$

In many elastic FWI applications for land problems, the least-squares misfit function is more sensitive to  $V_s$ , as shear events have strong imprint in the data. When considering significant geological heterogeneities such as alluvial deposits in the near-surface in Figure 3(a), the inversion process will be dominated by the  $V_s$  update in those low-velocity zones. This might lead to *unrealistic updates* where  $V_s > V_p$  or too small value of  $V_s$ . To overcome this issue, we introduce the constraint on the ratio  $V_p/V_s$ , which is applied simultaneously with the bound constraints on the range of  $V_p$  and  $V_s$ . The FWI problem now

can be considered as

$$\min_{\mathbf{m}} \chi(\mathbf{m}) \quad \text{where} \quad \mathbf{m} \in (C_1 \cap C_2). \quad (1)$$

The misfit function  $\chi(\mathbf{m})$  is minimized over a restricted model space, where the model should simultaneously satisfy two constraints:

- Bounds constraint  $C_1$ :  $V_p$  and  $V_s$  should vary within pre-defined ranges.
- Ratio constraint  $C_2$ : The ratio  $V_p/V_s$  should vary within a pre-defined range, for example  $V_p/V_s \in [1.4 - 3.0]$ .

These constraints can be designed based on well data or simple geological knowledge about the structure. The projection of model parameters onto the intersection of two constraints are performed through the Dykstra's algorithm, which ensures the uniqueness of the solution, independently with the order of the constraints application (Boyle and Dykstra, 1986; Peters and Herrmann, 2017).

### SEAM II FOOTHILL DIP-LINE CONFIGURATION

Our main target is the cross-section of the SEAM II Foothill model, underneath the pseudo-2D dip-line survey. We limit the investigated area at 8 km in the  $x$ -direction. The associated compressional and shear velocities are presented in Figure 3(a). The topography variation in this area is significant, with maximal vertical variation of 900 m as shown in Figure 1. The structure is characterized by gentle dip in the  $x$ -direction with folding structures and an unconformity at 2-3 km depth. The near-surface has alluvial deposits resulting from rapid erosion (Regone et al., 2017). These channels have low shear velocity, about 550 m/s at the surface, which are main obstacles for FWI. Moreover, the first 500 m below the surface has anelastic properties with  $Q_p = Q_s = 50$ .

The pseudo-2D line is acquired along the middle of the SEAM II Foothill model in the dip ( $x$ ) direction. Due to limited computational resources, we only treat 40 shots: their positions are indicated by black triangles in Figure 1, with inline source-spacing being 200 m. There are 9 parallel receiver lines: the central line lies along the source line, with 4 parallel lines on either side, spaced at 25 m in the crossline ( $y$ ) direction. Receivers in the inline direction are located each 6.25 m

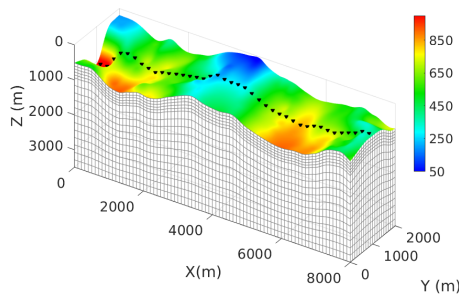


Figure 1: The 3D SEM mesh designed at 3 Hz maximal frequency. The topography map is put on top of the mesh, where the colorbar illustrates the absolute depth  $Z_{abs}$  (m) from a pre-defined zero-depth. The source positions of the 2D line are indicated by black triangles ( $\Delta S = 200$  m).

(Oristaglio, 2016). All of the receivers are 3-components geophones and the sources are vertical point-force.

The acquired visco-elastic data is complex, including highly energetic and dispersive surface waves, as shown in Figure 2(a). Significant back-scattering and converted waves are generated at the steep-slope positions and at the strong-contrast interfaces between the alluvial deposits and the background medium (Figure 2(c)). The reverberations inside the low-velocity channels also dominate the wavefield amplitude, which are the most challenging parts for data fitting.

### INVERSION SETUP

The data considered for our inversion are the ones generated by the SEAM consortium, for which we do not have information about the numerical method, the mesh design and the source wavelet. The application is therefore not in the inverse-crime configuration.

#### Initial models & Mesh design

The initial  $V_p$  and  $V_s$  models are built in a realistic way, from 5 logs at positions 0, 2, 4, 6 and 8 km in  $x$ -direction. The models are obtained from a standard interpolation between upscaling logs data, as shown in Figure 3(b). We assume that no precise information about the alluvial deposits is available, leading to a wrong near-surface description in the starting velocity models. The density model is calculated from  $V_p$  through the relationship:

$$\rho [\text{kg/m}^3] = 0.177 \times V_p [\text{m/s}] + 1663. \quad (2)$$

This is a linear regression obtained from wells data.

To account for the 3D propagation effect, we consider a narrow 3D model with 2 km in  $y$ -direction. Since we limit at 8 km

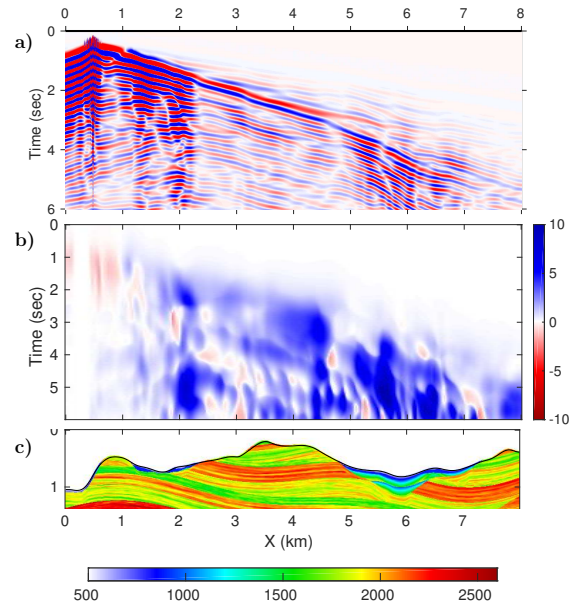


Figure 2: (a) The  $z$ -component of the observed visco-elastic data, low-pass filtered at 5 Hz. (b) Time envelope-misfit [%] between the simulated elastic and viscoelastic data, computed for the whole seismic gather: showing negligible difference. (c) The near-surface  $V_s$  model.

offset in  $x$ -direction, we do not expect any model update below 3.5 km in depth. The 3D initial models are built from these 2D sections assuming invariance along the  $y$ -direction.

Different SEM meshes are designed for different inversion frequency bands (i.e. 0-3 Hz and 0-5 Hz). Since we expect significant heterogeneities at the near-surface, the first 500 m in  $z$ -direction is filled with small elements. The element sizes are computed from the expected shear wavelength. An example of the mesh design for the maximal frequency at 3 Hz is shown in Figure 1. Each element is deformed by the 4<sup>th</sup>-order shape functions to describe the sharp topography (Trinh et al., 2018).

### 3D elastic inversion setup: Data-windowing hierarchy

We apply our FWI frame on SEAM II Foothill dataset, low-pass filtered in the [0-5 Hz] frequency band. The time-frequency envelope misfit (Fig. 2(b)) is used to compare the synthetic elastic and visco-elastic seismograms, showing negligible difference: less than 10% misfit (Kristeková et al., 2006). Based on this observation, we decide to use elastic engine to invert for the visco-elastic dataset, at least at low frequency. However, it is interesting to note that the main differences occur at surface and back-scattering waves at the alluvial deposits (Fig. 2(c)).

We invert simultaneously for  $V_p$  and  $V_s$ . To mitigate the dominance of the  $V_s$  parameter over  $V_p$ , due to the presence of surface waves, we use a two-steps data-windowing hierarchy: (1) The early-body waves, arriving before the surface waves, are first considered for the inversion. (2) The reconstructed models will then be used as starting models for the inversion with the whole wavefield. We simply use a bottom mute to separate the early-body waves with other parts of the wavefield. Each step contains different FWI sequences as will be detailed in the next sections. Each sequence contains 30 iterations, where the density and the source wavelet are kept unchanged. After each inversion sequence, the source wavelet is re-estimated and the density is computed from the obtained  $V_p$  model according to the empirical relationship (2).

We do not apply other preconditioning than the Bessel-based gradient smoothing (Trinh et al., 2017). The coherent lengths design is adapted to the working frequency:  $L_v = 100\text{m}$  and  $L_u = L_w = 400\text{m}$  for [0-3 Hz];  $L_v = 30\text{m}$  and  $L_u = L_w = 120\text{m}$  for [0-5 Hz]. We suppose that the smooth dip field is known and 0° strike as our main target is a 2D cross-section. In real applications, the dip can be extracted from a migrated image.

#### *Inversion with early-body waves*

When considering the early body-waves within the range [0-5 Hz], the calculated data computed from the initial models are cycle-skipped compared with the observed data at the far offsets. The cycle-skipping issue can be assessed by the time-lag attribute (Figure 4(a)), which measures the time-lag of the maximum of the cross-correlation function between the calculated and the observed windowed seismic traces. The attribute is computed for all traces acquired by the central receiver line. It should be noted that the synthetic data is considered as cycle-skipped when the measured time-shift with the observed data is more than 0.1 sec (half of the apparent wavelength in the observed data). Since the initial models have no information

about the low-velocity alluvial deposits, the cycle skipping is also visible for the near-offset data in these areas.

We apply the standard low-to-high frequency strategy (Bunks et al., 1995) by considering two frequency bands: [0-3 Hz] and [0-5 Hz]. For each frequency band, we firstly inject half of the early-body waves package in time. The recovered models will then be used as starting models for the inversion with all the early-body waves. This strategy helps to enhance the  $V_p$  estimation since the early arrivals have more P-wave signature. The final models after the inversion with the early-body waves are shown in Figure 3(c).

#### *Inversion with all the wavefield*

Since the seismic wavefield is dominated by surface waves and back-scattering energies (Figure 2(a)), we would like to incorporate these information into the inversion. The comparison of the entire wavefield between the calculated and the observed data indicates that the models in Figure 3(c) are not good enough to avoid the cycle-skipping issue at 5 Hz (The time-shift attribute map is not shown here). We then consider again the low-to-high frequency strategy by considering two frequency bands: [0-3 Hz] and [0-5 Hz].

Starting from the models 3(c), the  $V_p$  and  $V_s$  parameters obtained from the inversion with the entire wavefield within [0-3 Hz] are shown in Figure 3(d). We do not show the results obtained from the next frequency band [0-5 Hz] due to insignificant improvement.

## INVERSION RESULTS & DISCUSSIONS

After the first step with low-to-high frequency strategy on early-body waves, the inversion successfully recovers main structures of the P- and S-velocity models (Figure 3(c)). The alluvial deposits and near-surface heterogeneities are well detected on both  $V_p$  and  $V_s$ . The time-shift comparison between the observed and the calculated data on these models (Figure 4(b)) shows significant improvement compared with the measurement on the initial models (Figure 4(a)), both at near and far offsets. However, the  $V_s$  model contains discontinuous geological features due to shallow penetration of the shear component, the poor illumination of the pseudo-2D acquisition and the sparsity of the sources.

Considering the entire wavefield helps to improve the  $V_s$  model, without degrading the  $V_p$  estimation, as shown in Figure 3(d). The continuity of the near-surface features are strengthened and the deeper structures at 2 km depth are better resolved. This is due to the fact that the inversion can exploit the shear body waves hidden by the surface waves and back-scattering energies. However, we stop the second inversion step at 3 Hz since the obtained near-surface models are not good enough to explain the surface energies at 5 Hz. It should be noted that the model resolution is limited by a half of the local wavelength. The inversion thus cannot reconstruct sharp contrasts in the obtained velocity models, leading to the limited capacity to fit the back-scattering and surface energies in the data. This is also one of the main reasons why we consider the low-to-high frequency strategy instead of other surface waves inversion strategies, such as the layer stripping technique proposed by Masoni et al. (2016).

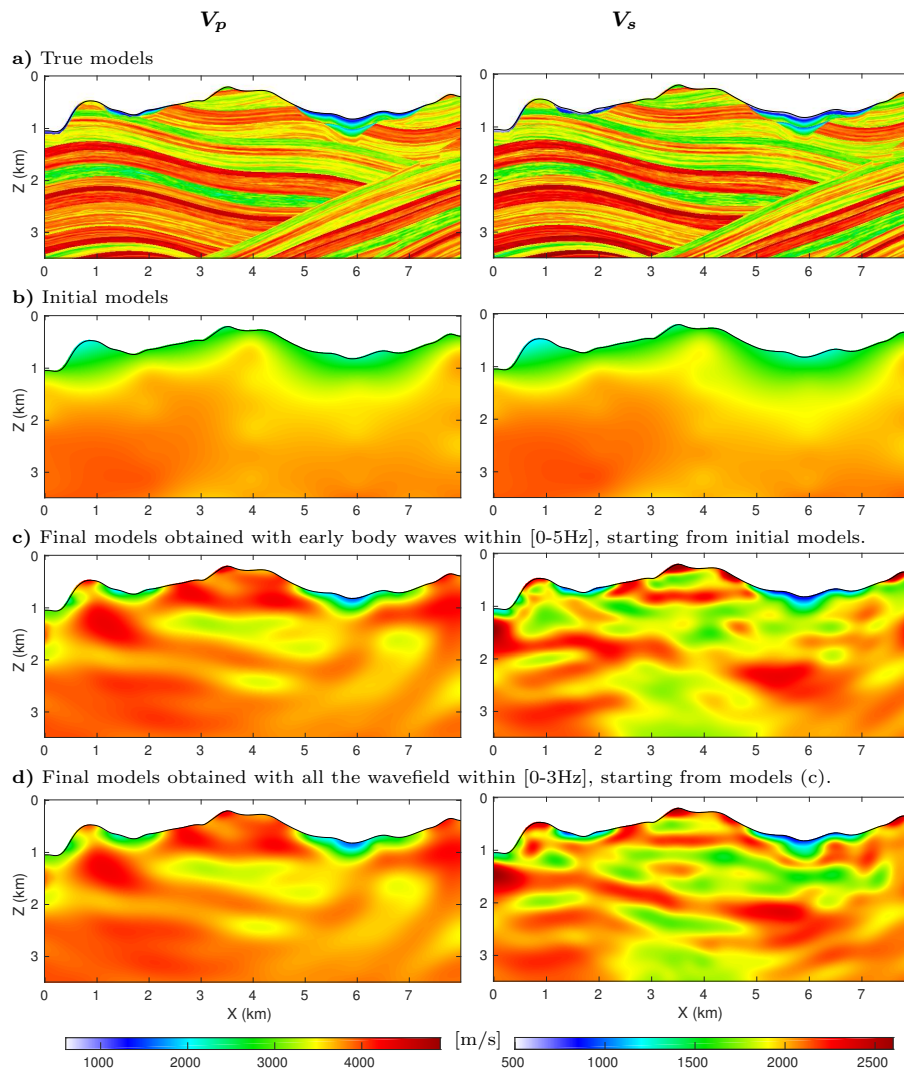


Figure 3: Left -  $V_p$  target cross-section, Right -  $V_s$  target cross-section: (a) True models. (b) Initial models. (c) Inversion results obtained with early-body waves within [0-5 Hz], showing interesting reconstruction for both  $V_p$  and  $V_s$ . (d) Inversion results by using all the wavefield within [0-3 Hz], showing improvement for the  $V_s$  estimation at depth.

Through our experiences, the model constraint on the ratio  $V_p/V_s$  is crucial for reliable simultaneous estimation of  $V_p$  and  $V_s$ , especially when strong heterogeneities are presented and/or poor illumination. Without this constraint, the inversion will stop after several iterations due to unrealistic updates at the near-surface.

## CONCLUSIONS AND PERSPECTIVES

The study illustrates the complexity of the data and elastic multi-parameter FWI problem in complex land areas. We use a two-steps data-windowing hierarchy and a model constraint on the ratio  $V_p/V_s$  to simultaneously invert for  $V_p$  and  $V_s$ . We treat body waves and surface energies independently, following low-to-high frequency strategies, to get a reliable model parameters estimation but also to exploit the maximum amount of information in the observed data. By being able to model surface waves and back-scattering energies, we can take advantage from the hidden information below these events to get

better  $V_s$  constraint, both at the near-surface and deeper parts. We also notice that body and surface waves require different frequency-hierarchy. In our example, higher model resolution is required before the [0-5 Hz] surface and back-scattering energies can be integrated into the inversion. The time-shift attribute can be used for model quality control but also for inversion hierarchy design. Perspectives include alternative misfits design and (visco-)elastic applications on real foothill dataset provided by TOTAL.

## ACKNOWLEDGMENTS

The authors would like to thank Total E&P for financial support of PTT's PhD project, and for allowing to present and access the SEAM II Foothill model. This study, partially funded by the SEISCOPE consortium (<http://seiscope2.osug.fr>), was granted access to the HPC resources of the CIMENT center (<https://ciment.ujf-grenoble.fr>), CINES/IDRIS/TGCC (allocation 046091 of GENCI) and Pangea (TOTAL S&A). Authors enjoy discussions with M. Appe, B. Duquet, J.L. Boelle and P. Williamson.

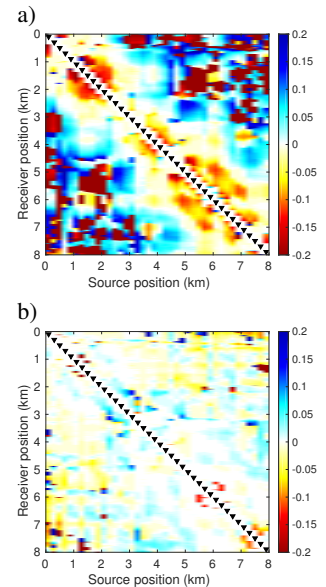


Figure 4: Time-shift maps [sec] between the calculated and the observed data. The attribute is computed for early-body waves within the range [0-5 Hz]: (a) From initial models; (b) From inverted models in Figure 3(c). Source positions are indicated by black triangles.

## REFERENCES

- Boyle, J. P., and R. L. Dykstra, 1986, A method for finding projections onto the intersection of convex sets in Hilbert spaces, in *Advances in Order Restricted Statistical Inference: Proceedings of the Symposium on Order Restricted Statistical Inference*, 28–47.
- Bunks, C., F. M. Salek, S. Zaleski, and G. Chavent, 1995, Multiscale seismic waveform inversion: *Geophysics*, **60**, 1457–1473, <https://doi.org/10.1190/1.1443880>.
- Cerjan, C. D., D. Kosloff, and M. Reshef, 1985, A non-reflecting boundary condition for direct acoustic and elastic wave equations: *Geophysics*, **50**, 705–708, <https://doi.org/10.1190/1.1441945>.
- Guittou, A., G. Ayeni, and E. Díaz, 2012, Constrained full-waveform inversion by model reparameterization: *Geophysics*, **77**, no. 2, R117–R127, <https://doi.org/10.1190/geo2011-0196.1>.
- Komatitsch, D., and J. Tromp, 1999, Introduction to the spectral element method for three-dimensional seismic wave propagation: *Geophysical Journal International*, **139**, 806–822, <https://doi.org/10.1046/j.1365-246x.1999.00967.x>.
- Kristeková, M., J. Kristek, P. Moczo, and S. Day, 2006, Misfit Criteria for Quantitative Comparison of Seismograms: *Bulletin of the Seismological Society of America*, **96**, 1836–1850, <https://doi.org/10.1785/0120060012>.
- Masoni, I., J.-L. Boelle, R. Brossier, and J. Virieux, 2016, Layer stripping FWI for surface waves: 86th Annual International Meeting, SEG, Expanded Abstracts, 1369–1373.
- Métivier, L., and R. Brossier, 2016, The SEISCOPE optimization tool-box. A large-scale nonlinear optimization library based on reverse communication: *Geophysics*, **81**, no. 2, F11–F25, <https://doi.org/10.1190/geo2015-0031.1>.
- Oristaglio, M., 2016, Land seismic challenges wraps up with Foothills model: *The Leading Edge*, **35**, 292–293, <https://doi.org/10.1190/tle35030292.1>.
- Peters, B., and F. J. Herrmann, 2017, Constraints versus penalties for edge-preserving full-waveform inversion: *The Leading Edge*, **36**, 94–100, <https://doi.org/10.1190/tle36010094.1>.
- Regone, C., J. Stefani, P. Wang, C. Gerea, G. Gonzalez, and M. Oristaglio, 2017, Geologic model building in SEAM Phase II—Land seismic challenges: *The Leading Edge*, **36**, 738–749, <https://doi.org/10.1190/tle36090738.1>.
- Stacey, R., 1988, Improved transparent boundary formulations for the elastic-wave equation: *Bulletin of the Seismological Society of America*, **78**, 2089–2097.
- Trinh, P. T., R. Brossier, L. Métivier, L. Tavard, and J. Virieux, 2018, Efficient 3D time-domain elastic and viscoelastic Full Waveform Inversion using a spectral-element method on flexible Cartesian-based mesh: 88th Annual International Meeting, SEG, Expanded Abstracts, 1533–1538.
- Trinh, P. T., R. Brossier, L. Métivier, J. Virieux, and P. Wellington, 2017, Bessel smoothing filter for spectral element mesh: *Geophysical Journal International*, **209**, 1489–1512, <https://doi.org/10.1093/gji/ggx103>.
- Yang, P., R. Brossier, L. Métivier, and J. Virieux, 2016, A review on the systematic formulation of 3D multiparameter full waveform inversion in viscoelastic medium: *Geophysical Journal International*, **207**, 129–149, <https://doi.org/10.1093/gji/ggw262>.